Superconductivity Behavior in Epitaxial TiN Films Points to Surface Magnetic Disorder

N.A. Saveskul,[1] N.A. Titova,[1] E.M. Baeva,[1,2] A.V. Semenov,[1] A.V. Lubenchenko,[3] S. Saha,[4,5] H. Reddy,[4,5] S.I. Bogdanov,[4,5] E.E. Marinero,[4,6] V.M. Shalaev,[4,5] A. Boltasseva,[4,5] V.S. Khrapai,[1,2,7] A.I. Kardakova,[1,2,*] and G.N. Goltsman[1,2]

[1] *Moscow State University of Education, 29 Malaya Pirogovskaya Street, Moscow 119435, Russia*
[2] *National Research University Higher School of Economics, 20 Myasnitskaya Street, Moscow 101000, Russia*
[3] *National Research University MPEI, Krasnokazarmennaya Street, 14, Moscow 111250, Russia*
[4] *School of Electrical & Computer Engineering and Birck Nanotechnology Center, Purdue University, 1205 West State Street, West Lafayette, Indiana 47907-2057, USA*
[5] *Purdue Quantum Science and Engineering Institute, Purdue University, West Lafayette, Indiana 47907, USA*
[6] *School of Materials Engineering, Purdue University, 1205 West State Street, West Lafayette, Indiana 47907-2057, USA*
[7] *Institute of Solid State Physics, 2 Ak. Osipyana Street, Chernogolovka 142432, Russia*

(Received 14 March 2019; revised manuscript received 15 July 2019; published 1 November 2019)

We analyze the evolution of the normal and superconducting properties of epitaxial TiN films, characterized by high Ioffe-Regel parameter values, as a function of the film thickness. As the film thickness decreases, we observe an increase of the residual resistivity, that becomes dominated by diffusive surface scattering for $d \leq 20$ nm. At the same time, a substantial thickness-dependent reduction of the superconducting critical temperature is observed compared to the bulk TiN value. In such high-quality material films, this effect can be explained by a weak magnetic disorder residing in the surface layer with a characteristic magnetic defect density of approximately 10^{12} cm^{-2}. Our results suggest that surface magnetic disorder is generally present in oxidized TiN films.

DOI: 10.1103/PhysRevApplied.12.054001

I. INTRODUCTION

Thin metallic films are exploited in numerous optical applications from nanophotonics and telecommunications at room temperature [1,2] to superconducting electronic devices at cryogenic temperatures [3,4]. Critical for optical and electronic applications, improving the film quality is a multifaceted problem that includes dealing with various disorder types that have different impacts on the electronic properties at ambient conditions and on the superconducting state. A classical example is the effect of paramagnetic impurities in metals, where a minute concentration of impurities can become detrimental at low temperature (T), resulting in a Kondo effect [5], the suppression of the superconducting gap [6], and a drastic enhancement of the inelastic scattering [7]. In thin films, a more important effect is produced by magnetic disorder formed spontaneously within oxidized native surface layers, which manifests in enhanced dephasing [8,9], Cooper-pair breaking [10,11], and magnetic flux noise [12,13].

Titanium nitride (TiN) thin films exhibit good chemical stability down to nanometer thickness [14] and are used in the fabrication of superconducting devices for photon detection [15] and for quantum-information processing [16–19]. Low dielectric losses at microwave frequencies observed in TiN films are associated with a relatively small surface density of two-level system defects that contribute to decoherence of the resonators and qubits [20–23]. In spite of a possible relation between the two-level systems and the magnetic disorder [24], the impact of the latter in TiN films is much less understood. Although the experiments do not exclude an unknown time-reversal symmetry-breaking mechanism in superconducting TiN [25], the interpretation is complicated by a high level of nonmagnetic disorder. Thin TiN films, typically fabricated for superconducting devices, are characterized by a relatively small Ioffe-Regel parameter of $k_F l \lesssim 10$, where k_F is the Fermi wave vector and l is the carrier mean free path. Thus, a gradual suppression of the superconductivity in thin films is attributed to the interplay of disorder and interactions [26–29] or the Berezinskii-Kosterlitz-Thouless phase transition [30]. In order to clarify the role of the magnetic disorder in thin films, one needs to isolate

*kardakova@rplab.ru

this effect by studying epitaxial films exhibiting excellent electrical properties.

In this work, we focus on the electronic and superconducting properties of the epitaxial TiN films with an exceptionally low level of nonmagnetic disorder, $k_F l \sim 500$. At decreasing film thickness (d) in the range $200 > d > 3$ nm, we observe an almost tenfold increase of the residual resistivity, which manifests a predominant contribution of diffusive surface scattering for films thinner than 20 nm. At the same time, the superconducting critical temperature in thin films is reduced by over a factor of 3 when compared to the bulk value in TiN. In contrast to previous experiments, the high structural and thus electrical quality of the materials studied allows us to rule out the possible impact of nonmagnetic disorder on the superconductivity. We theoretically confirm that a minute amount of magnetic scattering centers, which reside mainly near the surface of the film and which are irrelevant to normal state transport, can account for the suppression of the superconductivity of small-thickness films. Our results imply that magnetic defects with a surface density of about 10^{12} cm^{-2} reside within the naturally oxidized top layer of TiN, similarly to other materials [8–13].

II. FABRICATION AND MEASUREMENT SETUP

TiN films are grown on a $\langle 111 \rangle$ c-sapphire substrate at a temperature of 800°C by dc reactive magnetron sputtering from a 99.999% pure Ti target. The growth is performed in an argon-nitrogen environment at a pressure of 5 mTorr and an Ar : N_2 flow ratio of 2:8 sccm. The films with different d values are divided chronologically in two sets (1 and 2), each set grown without opening the chamber. Between the two growth processes, the chamber is opened and the Ti target replaced. Between the subsequent TiN runs during the deposition period, no other material is deposited.

The electronic properties of the unpatterned TiN films from the two sets are obtained by means of variable-angle spectroscopic ellipsometry [31] at room temperature (data for plasma frequency ω_p) and also by resistance measurement in a homemade ^{4}He variable temperature insert and a cryodilution refrigerator. The resistance measurements are carried out with a 370 AC Lake Shore resistance bridge at a bias current of 316 nA or less.

Sheet resistance $R_s^{300\ \mathrm{K}}$ of films with $d = 3, 10, 100$ nm is measured by the van der Pauw method at room temperature. The T dependencies of resistance $R(T)$ and $RRR = R^{300\ \mathrm{K}}/R^{10\ \mathrm{K}}$ are measured in a quasi-four-probe configuration. At low T, $R_s^{10\ \mathrm{K}}$ is extracted using the relation $R_s^{10\ \mathrm{K}} = R_s^{300\ \mathrm{K}} RRR^{-1}$. Films with $d = 4, 5, 20, 200$ nm are patterned in Hall bridges, and $R_s(T)$ with RRR are investigated in a four-probe configuration. The uncertainty in the measurement of $R_s^{300\ \mathrm{K}}$ is determined from the statistics in different samples of the same thickness.

III. RESULTS AND DISCUSSION

The epitaxial TiN films are known to exhibit single-crystalline order [32,33]. In the following, we start from a demonstration of the exceptional metallic properties of our films and investigate the electron-phonon scattering and disorder scattering contributions to the film resistivity. This enables us to evaluate the thickness of the oxide ("dead") layer on the surface of the film and the d-dependent mean free path at low T. Next, we study the superconducting properties and analyze the suppression of the superconducting critical temperature T_c with decreasing film thickness. Using the Abrikosov-Gorkov theory [6], we estimate the density of the magnetic defects in fabricated films and observe that in the thin-film limit, the magnetic disorder has a predominantly surface origin. The electronic properties of the films are summarized in Table I.

Structural characterization of our TiN films is summarized in Fig. 1. In the body of panel Fig. 1(a), we plot the x-ray diffraction data for a coupled $\omega - 2\theta$ scan of a 20-nm TiN film. Here, we identify and mark by the vertical arrows the two main reflexes of TiN (111) and Al_2O_3 (0006), respectively, for the film and for the substrate. The gray-scale plot in the inset demonstrates that both these reflexes (marked by the same arrows) correspond to localized points in the reciprocal space, evidencing that our epitaxial TiN films are monocrystalline. In Fig. 1(b), we plot the atomic-force-microscope (AFM) image of a 5-nm-thick TiN film and its substrate along with the representative cuts. The root-mean-square surface roughness

TABLE I. Parameters of the TiN films.

	d (nm)	$R_s^{300\ \mathrm{K}}$ (ohm/sq)	RRR	T_c (K)	ξ_0 (nm)	ω_p(300 K) (eV)	τ_{tr}(10 K) (fs)	l(10 K) (nm)
Set 1	20	9.8 ± 1.0	3.2	5.6	22	7.02	18	8.0
	10	26.6 ± 2.3	2.2	4.5	22	6.85	11	5.5
	5	103 ± 6.3	1.7	3.8	20	6.44	7	3.5
Set 2	200	0.99 ± 0.2	7.0	4.5	41	6.41	43	19
	100	1.9 ± 0.1	6.2	4.5	42	6.97	33	17
	4	130 ± 18.5	1.9	1.9	31	7.01	6	3.5
	3	264 ± 14.5	1.5	1.4	26	7.02	4	2.2

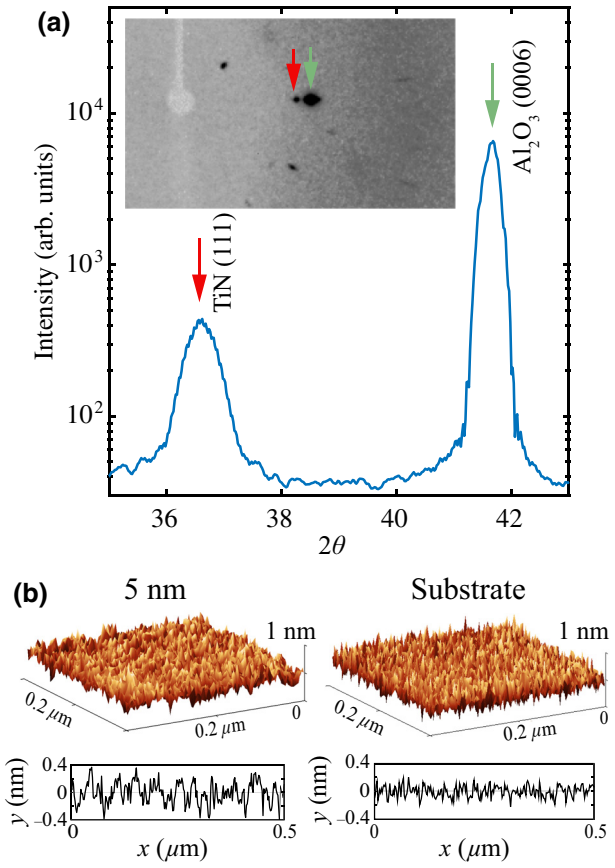

FIG. 1. Characterization of the epitaxial TiN films. (a) X-ray diffraction study of a 20-nm TiN film. Body: Coupled $\omega - 2\theta$ scan, obtained with a Shimadzu XRD-7000 S diffractometer (Cu source, $K_{\alpha 1} = 1.5406$ Å). Inset: Gray-scale reciprocal space map obtained with an Oxford diffraction Gemini R diffractometer (Mo source, $K_{\alpha 1} = 0.7093$ Å) for $\Delta\omega = 3°$ around the central value of $\omega = 9.05°$. In both plots, the vertical arrows mark the positions of the TiN (111) reflex from the film and the (much stronger) Al_2O_3 (0006) reflex from the sapphire substrate. (b) AFM images of the 5-nm TiN film (on the lhs) and the sapphire substrate (on the rhs) along with the corresponding representative cuts. The rms roughness of the TiN film is below 0.25 nm, which corresponds to the atomically smooth surface.

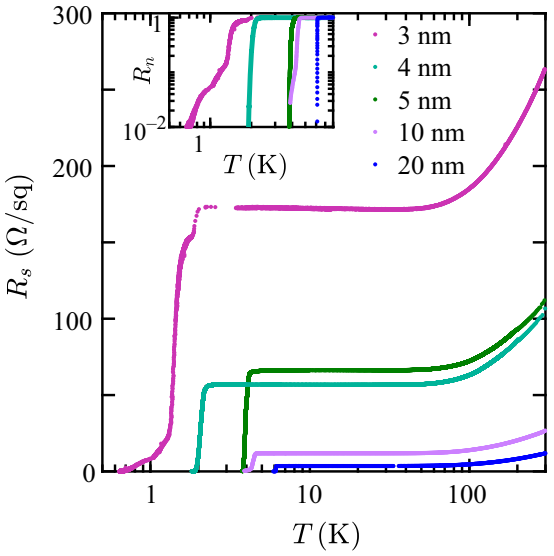

FIG. 2. The temperature (T) dependence of sheet resistance (R_s) for five films with different thicknesses: 20 nm (set 1), 10 nm (set 1), 5 nm (set 1), 4 nm (set 2), and 3 nm (set 2). Body: The $R_s(T)$-dependence in the wide T range. The critical temperatures of transition to the superconducting state are 5.6, 4.5, 3.8, 1.9, and 1.4 K for 20, 10, 5, 4, and 3 nm, respectively. Inset: The $R(T)$ dependence for the TiN films at low temperatures in the log-log scale. The data are obtained with a (quasi) four-probe method; the bias current is 316 nA.

of the TiN film is below 0.25 nm, which corresponds to an atomically smooth surface. Details of additional x-ray photoelectron spectroscopy (XPS) of our samples are given in the Supplemental Material [34]. The XPS results are obtained on the basis of the method described in Ref. [35].

Figure 2 summarizes the electronic transport properties of the fabricated TiN films of different thicknesses. Here, we plot the experimental T dependencies of the sheet resistance R_s for TiN films in zero magnetic field. At decreasing T, the R_s initially drops linearly and saturates at a residual resistance below about 50 K. This linear-in-temperature behavior is fully consistent with the high-T asymptote of the Bloch-Grüneisen formula that holds in normal metals down to temperatures $T \propto \theta_D/3$ [36], where θ_D is the Debye temperature. Our estimate of θ_D for TiN is in the range of 480–600 K (see Supplemental Material [34] for details), in agreement with the previously reported values [37]. This metallic behavior is typical for all studied films and reveals a substantial electron-phonon scattering contribution down to a few-nanometer film thickness. The residual resistance ratio, listed in Table I, reaches $RRR = 7$, emphasizing the high quality of the films. The room-temperature resistivity $\rho^{300\ \mathrm{K}} \equiv R_s^{300\ \mathrm{K}} d$ attains values as low as $\rho^{300\ \mathrm{K}} \sim 20\ \mu\Omega\,\mathrm{cm}$ for $d \geq 100$ nm, which is similar to the best reported results in thin films [14,38] as well as in a thick single crystal [37]. This similarity is not surprising given the fact that $\rho^{300\ \mathrm{K}}$ is determined by the phonon scattering, rather than disorder, once again emphasizing the quality of the material and its conceptual difference from the disordered TiN films investigated in most previous works [25,30,39].

We now investigate the electron-phonon (e-ph) interaction in our films in more detail, which allows us to evaluate the thickness of the dead layer on the surface of the films and understand the d dependence of the e-ph coupling strength. In Fig. 3(a), we analyze the phononic contribution to the TiN film conductance at room temperature, defined as $G_{\mathrm{ph}}^{300\ \mathrm{K}} = (R_s^{300\ \mathrm{K}} - R_s^{10\ \mathrm{K}})^{-1}$. Plotted as a function of d, the $G_{\mathrm{ph}}^{300\ \mathrm{K}}$ shows a linear dependence with a finite intercept around $d_{\mathrm{DL}} \approx 1.9 \pm 0.5$ nm for set 1 (see the guideline). In other words, the phonon-induced conductance scales

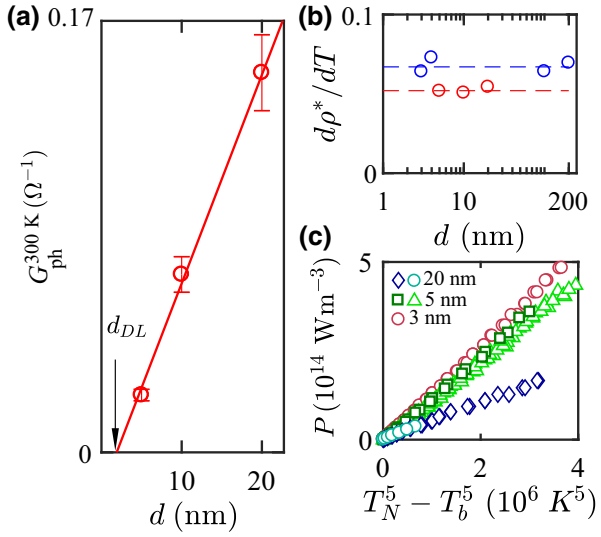

FIG. 3. The analysis of the strength of the electron-phonon (e-ph) coupling with film thickness decrease. (a) The thickness dependence of the electron-phonon contribution to the conductance, $G_{ph}^{300\ K} = (R_s^{300\ K} - R_s^{10\ K})^{-1}$. The linear fit of these data provides the estimate of the thickness of an insulating dead layer at the surface of the TiN film: $d_{DL} = 1.9$ nm. (b) The slope of the high-T linear part of the T dependence of the resistivity as a function of d. The resistivity is corrected for the finite dead-layer thickness as $\rho^*(T) = R_s(d - d_{DL})$. The data indicate a minor variation of the strength of the electron-phonon scattering in the two sets (red dots are for set 1 and blue dots for set 2). (c) The heat power flow, normalized to volume, versus $(T_e^5 - T_b^5)$, where T_N is the noise temperature and T_b the bath temperature. The data are obtained for five samples with thicknesses of 20, 5, and 3 nm.

linearly with d^*, where $d^* = d - d_{DL}$, indicating that a minor size effect observed in $G_{ph}^{300\ K}$ versus d is consistent with a trivial decrease of the effective film thickness. Most likely, the insulating dead layer at the surface of our TiN films consists of a mixture of titanium oxide and oxynitride [40,41]. The presence of such a dead layer is consistent with the XPS spectra (see Supplemental Material Table 1 [34] for the XPS film profile). As shown in Fig. 3(b), where we plot the slope of the high-T linear part of the T dependence of the resistivity as a function of d, the correction for the dead-layer thickness, introduced as $\rho^* = R_s d^*$, is capable of accounting for the observed d dependence of the (e-ph) scattering in both film sets.

Further insight into the e-ph coupling at low temperatures, in the residual resistance range, is obtained via noise thermometry [42]. In this experiment, five bridge samples made of 3-, 5-, and 20-nm-thick films are dc biased and the resulting noise temperature (T_N) is measured with the help of a homemade noise amplification stage (see Fig. 6 in Appendix A for the details). The dependence of the T_N on the joule power per unit volume, P, is demonstrated in Fig. 3(c). This dependence is very well described by the heat outflow law $P = \Sigma_{e\text{-ph}}(T_N^5 - T_b^5)$, where T_b is the bath temperature and $\Sigma_{e\text{-ph}}$ is the effective e-ph coupling. The exponent of 5 in this expression corresponds to the case of e-ph relaxation in clean metals. The measured $\Sigma_{e\text{-ph}}$ increases at decreasing d from 20 to 3 nm, roughly by a factor of 2 or even stronger, if one takes the finite d_{DL} into account. Note that $\Sigma_{e\text{-ph}}$ is directly proportional to the coupling strength in the BCS theory of the superconductivity [43]. As such, the noise thermometry indicates stronger BCS coupling in thinner films, which is the opposite of the trend observed in T_c as a function of d in the data of Fig. 2. This conclusion is important for our discussion of the superconducting properties below.

Unlike the case of e-ph conductance $G_{ph}^{300\ K}$, the analysis of residual resistivity reveals a much stronger size effect in the dependence of the film thickness. At low T, the mean free path increases and we observe the size effect at decreasing d, with a transition from the dominant bulk scattering in thick films to the surface scattering in thin films. Figure 4 shows that, in both sets, the residual resistivity measured at $T = 10$ K increases at least by a factor of

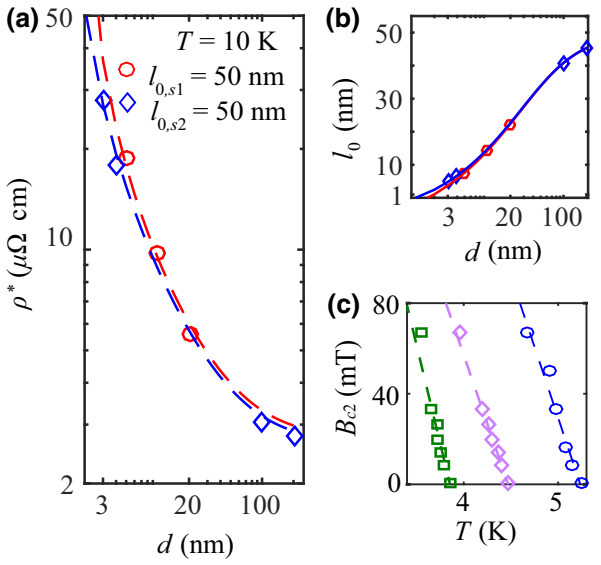

FIG. 4. Size effect in the residual resistivity. (a) Resistivity as a function of film thickness. The red circles correspond to the data for set 1 and the blue diamonds to set 2. The values of resistivity are corrected assuming the dead layer to be $\rho_0^* = R_s^{10\ K}(d - d_{DL})$. The red and blue dashed lines are fits for the FS model [Eq. (1)] assuming diffusive surface scattering. (b) The disorder-limited mean free path $l = l_0\rho_0^*/\rho^*$ in TiN films (shown by symbols) as a function of d, along with the FS-based fits for the two sets. (c) The typical T dependencies of the second critical magnetic field B_{c2} for three films with different thicknesses: 5, 10, and 20 nm (set 1, from left to right). The $B(T)$ dependencies are obtained from the shift of the superconducting transition temperature in a perpendicular magnetic field identified as the point where the resistance is half that of a normal state. These data are used to determine the Ginzburg-Landau superconducting coherence length ξ_0 at $T = 0$ K.

4 for decreasing d. Assuming diffusive surface scattering, we fit the data using the Fuchs-Sondheimer (FS) model [44,45]:

$$\frac{\rho_0^*}{\rho^*} = 1 - \frac{3l_0}{2d^*}\int_1^\infty \left(\frac{1}{t^3} - \frac{1}{t^5}\right)(1 - e^{-td^*/l_0})\,dt, \qquad (1)$$

where $d^* = d - d_{\mathrm{DL}}$ and the fit parameters l_0 and ρ_0^* are, respectively, the mean free path and the resistivity in the thick-film limit. The best fits shown by the dashed lines in Fig. 4(a) correspond to $l_0 = 50 \pm 5$ nm and $\rho_0^* = 2.7 \pm 0.2\ \mu\Omega\,\mathrm{cm}$ for set 1 and $l_0 = 50 \pm 5$ nm and $\rho_0^* = 2.6 \pm 0.2\ \mu\Omega\,\mathrm{cm}$ for set 2. This procedure allows us to evaluate the d-dependent mean free path $l = l_0\rho_0^*/\rho^*$ in our films, shown by symbols in Fig. 4(b), and estimate the Ioffe-Regel parameter as high as $k_F l_0 = \sqrt{3\pi^2\hbar l_0/e^2\rho_0^*} \approx 500$ in the thick-film limit. This estimate is two times bigger than the mean free paths obtained independently from the data on the transport relaxation time and diffusion coefficient extracted from the measured ρ^*, plasma frequency ω_p, and the Ginzburg-Landau superconducting coherence length (see Table I). The plasma frequency is measured by ellipsometry at room temperature, and the coherence length is determined using the relation $(\xi_0)^2 = -\Phi_0(dB_{c2}/dT)^{-1}/2\pi T_c$ from the temperature dependencies of the second critical magnetic field $B_{c2}(T)$; see Fig. 4(c). The transport relaxation time is estimated as $\tau_{\mathrm{tr}} = 1/(\rho^{10\ \mathrm{K}}\omega_p^2\varepsilon_0)$, assuming that ω_p is temperature independent [46]. In our analysis of the size effect in the residual resistance, we exclude the Mayadas-Shatzkes (MS) model [47], which focuses on the scattering of electrons at grain boundaries in polycrystalline thin films. The negligible granularity in our epitaxial films directly follows from our XRD and topography data in Fig. 1. Consistently, when applied to our data, the MS model returns a negligible contribution of scattering at grain boundaries (see Fig. 3S in the Supplemental Material [34] for the details).

We conclude the transport studies in the normal state of our TiN films by evaluating the charge carrier density, n, from the product $\rho^* l$. In the spirit of Ref. [14], we use the FS model fits of Fig. 4(a) and the free-electron expression [45] $\rho\, l = (3\pi^2)^{1/3} n^{-2/3}\hbar/e^2$, where $\hbar$ is the Planck constant and e is the elementary charge. In this way, we obtain $n \approx 2.9 \times 10^{22}\ \mathrm{cm}^{-3}$, which is the same order of magnitude compared to the density $n = 8 \times 10^{22}\ \mathrm{cm}^{-3}$ expected for a single electron per Ti atom, as well as to the experimental value of $n \approx 5 \times 10^{22}\ \mathrm{cm}^{-3}$ obtained from the Hall effect measurements in nominally identical films [31]. This observation is also consistent with the fact that the Bloch-Grüneisen temperature is close to the Debye temperature in our analysis of the e-ph scattering (see Fig. 4S of the Supplemental Material [34]), which excludes a diluted metal scenario [48]. Altogether, our analysis does not support the conclusions of Ref. [14] that the charge transport in epitaxial TiN films is dominated by the minority carriers from slightly filled bands.

Next, we analyze the superconducting properties of the fabricated TiN films. We observe a sharp transition to the superconducting state that occurs below a few kelvins at $T = T_c$; see the inset in Fig. 2. For simplicity, we determine the critical temperature T_c in Table I as the point where the resistance is half that of $R_s^{10\ \mathrm{K}}$. Note that the variation of T_c in the experiment by far exceeds the width of the resistive transition; therefore, the results discussed below are insensitive to the criterion used to define the transition point [49]. In both sets, the T_c values considerably diminish as d is reduced. The critical temperature is systematically lower within set 2 and varies by more than a factor of 3 for the thinnest films (see Table I). Note that the effect of decreasing T_c occurs in high-quality films with $R_s \ll \hbar/e^2$; that is, the films are far away from the superconductor-insulator transition [27]. In this case, the nonmagnetic disorder does not affect T_c. Thus, we also exclude the Berezinskii-Kosterlitz-Thouless phase transition [30] and the impact of Coulomb interactions [50], responsible for a decrease of T_c in thin dirty superconducting films (see Fig. 7 in Appendix B for details). We also eliminate possible effects of the reduced carrier density and/or BCS-coupling strength in thin films [51,52], because the observed trends in ω_p (Table I) and the e-ph coupling [Figs. 3(b) and 3(c)] are absent or opposite to that for T_c.

Both the observed differences in T_c between the two sets and its decrease upon the reduction of d can be explained by the presence of a minute amount of magnetic disorder, which has a well-known detrimental effect on T_c owing to pair-breaking spin-flip scattering [6]. The spin-flip scattering time τ_s and the critical temperature of the superconducting transition T_c are related via the Abrikosov-Gorkov (AG) equation [6,53]:

$$\ln\left(\frac{T_c^0}{T_c}\right) = \psi\left(\frac{1}{2} + \frac{\hbar}{2\pi k_B T_c^0 \tau_s}\right) - \psi\left(\frac{1}{2}\right), \qquad (2)$$

where $\psi(x)$ is the digamma function, and T_c^0 is the critical temperature in the absence of magnetic disorder. The solid line in the inset of Fig. 5 demonstrates the dependence of the normalized T_c as a function of the normalized spin-flip rate $x = \hbar/(2\pi k_B T_c^0 \tau_s)$ given by Eq. (2). This dependence is used to extract the spin-flip rate from the measured T_c for each TiN film studied.

For both sets of samples, we assume the same $T_c^0 = 6$ K, which is the highest reported value of the critical temperature in TiN [37]. Figure 5 (body) presents the dependence of the spin-flip scattering rate τ_s^{-1} as a function of an inverse thickness d^{-1}. Note that the timescale of τ_s falls in the range of 1–15 ps, which is roughly 3 orders of magnitude longer compared to the transport scattering time τ_{tr} for

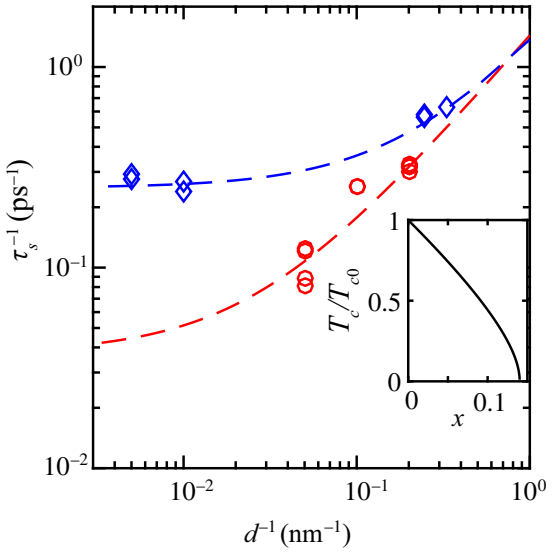

FIG. 5. The illustration of a detrimental effect of magnetic disorder on T_c in thin films. Body: The estimated spin-flip scattering rate τ_s^{-1} as a function of an inverse thickness $1/d$. Inset: The solid line demonstrates the dependence of the normalized T_c as a function of the normalized spin-flip rate $x = \hbar/(2\pi k_B T_c^0 \tau_s)$ given by Eq. (2). This dependence is used to convert the measured T_c for each studied TiN film to the spin-flip rate. The fitting of the data (τ_s^{-1} vs d^{-1}) demonstrates that the dominant contribution to the spin-flip scattering in thin films originates from the near-surface magnetic disorder: $N_M \sim a/(v_F\tau_s) = N_b + N_s \times a/d$, where $a \approx 0.4$ nm [54] is the TiN lattice constant, v_F is the Fermi velocity, N_b and N_s are the effective bulk and the surface number of the magnetic scatterers, respectively. The dashed lines demonstrate the best fits for the two sets, obtained with the bulk defect number of $N_b = 3 \times 10^{-5}$ for set 1 and $N_b = 2.5 \times 10^{-4}$ for set 2 and the surface defect number of $N_s = 2.8 \times 10^{-3}$, the same for both sets.

scattering off the nonmagnetic disorder (Table I). Therefore, we once again exclude the role of the nonmagnetic disorder in the scaling of transition temperatures in thin films.

Figure 5 demonstrates that the spin-flip scattering rate increases at decreasing d. We argue that this is consistent with the surface magnetic disorder that dominates in thin films. For $d < \xi_0$, the superconductivity is sensitive to the total volume density of the magnetic scatterers regardless of their distribution within the cross section of the film. Hence, the d dependence of the τ_s^{-1} indicates that extra spin-flip scattering in thin films originates from the magnetic disorder residing near the surface.

We apply a simplified theoretical model capable of qualitatively reconciling our data. Using the data of Fig. 5, we extract the effective density of the magnetic scatterers N_M, including the bulk N_b and the surface N_s contributions explicitly. It is convenient to normalize the numbers N_M, N_b, and N_s, respectively, per three-dimensional (3D) and two-dimensional (2D) unit cells in TiN, such that $N_M = N_b + N_s \times a/d$, where $a \approx 0.4$ nm [54] is the TiN lattice constant. The relation between the N_M and the spin-flip scattering rate reads $N_M \sim a/(v_F\tau_s)$, where v_F is the Fermi velocity. The dashed lines in Fig. 5 demonstrate the best fits for the two sets, obtained with $N_b = 3 \times 10^{-5}$ for set 1, $N_b = 2.5 \times 10^{-4}$ for set 2, and $N_s = 2.8 \times 10^{-3}$, the same for both sets. These estimates are obtained using the average value of the Fermi velocity $v_F \approx 4 \times 10^7$ cm/s extracted from experimental values of electron diffusivity D and the electron scattering time τ_{tr} as $v_F \sim \sqrt{D/\tau_{tr}}$ (see Fig. 5S in the Supplemental Material [34]). While different values of N_b can account for a growth-related variation between the sets, the same value of N_s indicates that the observed drop of T_c at decreasing d is an important systematic effect in thin epitaxial TiN films. The values of N_s provide us with an estimate of the surface density of magnetic defects that is as small as $a^{-2}N_s = 10^{12}$ cm^{-2}, at least an order of magnitude smaller in comparison with the typical density of the surface magnetic moments (approximately 5×10^{13} cm^{-2}), reported for Al, Nb, and NbN superconductors [13,24,55–57]. Note, however, that relevant for the T_c reduction are only those magnetic scatterers that strongly couple to the conduction electrons. This could, at least partly, explain the very small density of the surface magnetic disorder obtained in our analysis.

Finally, we discuss the possible microscopic origin of the surface magnetic disorder. It should be noted that magnetic materials are never used in the TiN growth chamber; therefore, a trivial contamination with paramagnetic impurities is excluded in the studied films. The surface character of the magnetic scattering in thin films indicates the importance of the TiN interfaces either with the substrate on the bottom or with the dead layer on the top. Similar to the observations in copper [7,8], aluminum [13], and niobium [11] films, we propose that the naturally oxidized top layer can be responsible for the magnetic disorder in our films. The magnetic moments in this case can originate from the unpaired $3d$ electrons bound to Ti^{+3}-O_V defect complexes [58], where O_V is the oxygen vacancy, which can result even in a room-temperature ferromagnetism in TiO_2 [59–62]. Recently, a long-range magnetic ordering in nonstoichiometric epitaxial TiN_{1-x} with $x = 0.12 \pm 0.02$ was revealed in Ref. [63], which originates from the Ruderman-Kittel-Kasuya-Yosida (RKKY) interaction between the unpaired localized spins mediated by nitrogen vacancies. Such spins, yet in much smaller concentration, can also be considered as possible magnetic scatterers in our TiN films, both in bulk and on the surface. In the end, it is worth mentioning that in our analysis of the T_c reduction at decreasing d, we ignore peculiarities of the band structure in TiN, which is argued to be a correlated material close to the Mott-insulator phase transition point [54]. Possible interplay between the band structure and magnetic disorder in thin TiN films is an intriguing target for future experiments.

IV. CONCLUSIONS

In summary, we analyze the electronic properties of the epitaxial TiN films of exceptional quality ($k_F l \sim 500$), which exhibit a size effect in resistivity and the reduction of the superconducting critical temperature with decreasing film thickness. The high structural and electronic quality of the films allows us to relate the latter effect to the presence of a minute concentration (approximately 10^{12} cm^{-2}) of magnetic scatterers within the approximately 2-nm-thick dead layer on the top of TiN films. The observed surface magnetic disorder can be related to the oxygen vacancies in naturally oxidized TiN films, representing a fundamental limiting factor for their performance in the superconducting state.

ACKNOWLEDGMENTS

We acknowledge valuable discussions with P. I. Arseev, M. V. Feigelman, T. M. Klapwijk, D. V. Shovkun, and M. A. Skvortsov. We are grateful to S. V. Simonov and S. L. Shestakov for their assistance with the x-ray studies, and N. S. Kaurova for her assistance with the AFM measurements. The authors also acknowledge N. Dilley for preliminary measurements of superconducting critical temperatures and critical fields in the TiN films. The Purdue team acknowledges support from the U.S. Department of Energy, Office of Basic Energy Sciences, Division of Materials Sciences and Engineering under Award DE-SC0017717 (growth of TiN films and measurement of plasma frequency). The transport and noise measurements are funded by the Russian Science Foundation project number 17-72-30036. The reciprocal state map of Fig. 1(a) is obtained within the state task of the ISSP RAS. The surface analysis (AFM and XPS) is funded by RFBR project number 16-29-11779. The theoretical analysis is supported by the Grant of the President RF No. MK-1308.2019.2.

APPENDIX A: STUDY OF ELECTRON-PHONON HEAT TRANSFER IN EPITAXIAL TIN FILMS

The noise thermometry is used to study the heat transfer between the electron system and the heat bath in the normal state of superconducting materials [42]. In such measurements, the sample is biased with a dc current that causes joule heating of the electronic system, and thereby the noise increases. The noise temperature T_N, obtained from the Johnson-Nyquist relation, $S_I = 4k_B T_N/R$, is considered as the electron temperature T_e, and the phonon temperature $T_{\rm ph}$ is taken as the bath temperature T_b.

For samples with length $L > l_{e\text{-ph}}$, where $l_{e\text{-ph}}$ is the electron-phonon length, the heat outflow rate can provide information about the electron-phonon interaction. The data in Fig. 6 are presented for a sample with a thickness of 5 nm. For the samples, the experimental data follow the heat outflow law, $P_{\rm dc} = \Sigma_{e\text{-ph}} V(T_N^n - T_b^n)$, where $P_{\rm dc}$ is

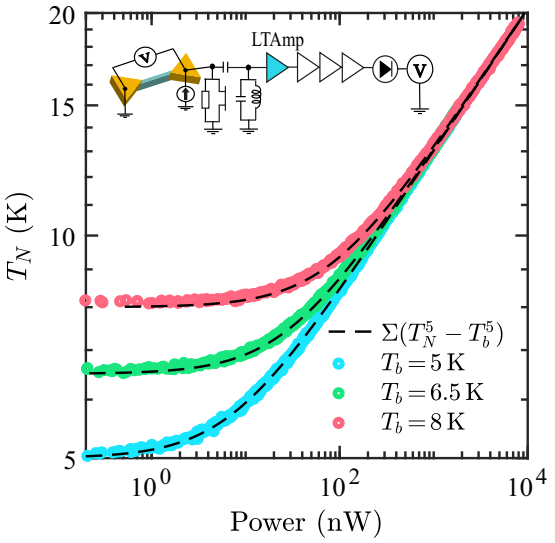

FIG. 6. Study of electron-phonon heat transfer in epitaxial TiN films. Body: The noise temperature T_N versus Joule power $P_{\rm dc}$. The data are presented for samples with thicknesses of 5 nm. Inset: The experimental setup for noise thermometry.

the Joule power dissipated in the sample, V is the volume of the sample, and $\Sigma_{e\text{-ph}}$ is the electron-phonon coupling constant. We observe that the exponent in the heat flow law is $n \simeq 5$ for all samples, which is typical for the case of pure metals and in the absence of a phonon bottleneck effect.

An experimental setup for noise thermometry is presented in the insert of Fig. 6. The setup, built inside

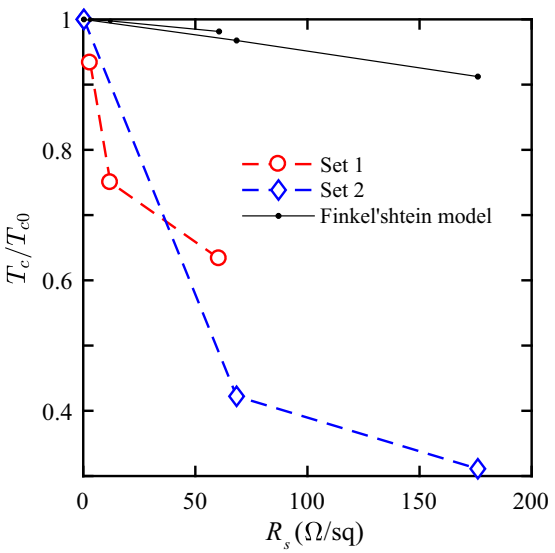

FIG. 7. Disorder effects on critical temperature: plot of the ratio T_c/T_{c0} as a function of the film resistance per square R_s. Data R_s are determined above the superconducting transition (at 10 K). The data are compared with the Finkel'stein model for the case of weak disorder in homogeneous superconducting films. The used model parameters are $\gamma \approx 6.7$ and $\tau = l^2/(ND) \approx 60$ fs.

a closed cycle refrigerator Bluefors LD-400, consists of a rf resonant-tank circuit (with a resonance frequency of 10 MHz) including a high-impedance low-noise amplifier at the 4-K stage (with gain > 6 dB and noise $S_{\text{amp}} \sim 10^{-26}$ A^2/Hz), a cascade of low-noise amplifiers at 300 K, an active band-pass filter, and a power detector.

APPENDIX B: DISORDER EFFECTS ON CRITICAL TEMPERATURE

We compare our results with predictions of a weak disorder model in homogeneous superconducting films established by Finkel'stein [50] (see Fig. 7). The suppression of superconductivity is driven by impurities that reinforce Coulomb and spin interactions. The critical temperature T_c is expressed as a function of sheet resistance R_s and the elastic diffusion time τ:

$$\frac{T_c}{T_{c0}} = e^{\gamma}\left(\frac{1/\gamma - \sqrt{t/2} + t/4}{1/\gamma + \sqrt{t/2} + t/4}\right)^{1/\sqrt{2t}}, \qquad \text{(B1)}$$

with $t = R_s e^2/(\pi h)$, $\gamma = ln[h/(k_B T_{c0}\tau)]$, and $T_{c0} = 6$ K (for set 1) or $T_{c0} = 4.5$ K (for set 2).

[1] S. A. Maier, *Plasmonics: Fundamentals and Applications* (Springer, New York, 2007).

[2] A. Catellani and A. Calzolari, Plasmonic properties of refractory titanium nitride, Phys. Rev. B **95**, 115145 (2017).

[3] W. Chang, S. M. Albrecht, T. S. Jespersen, F. Kuemmeth, P. Krogstrup, J. Nygard, and C. M. Marcus, Hard gap in epitaxial semiconductor–superconductor nanowires, Nat. Nanotechnol. **10**, 232 (2015).

[4] R. Yan, G. Khalsa, S. Vishwanath, Y. Han, J. Wright, S. Rouvimov, D. S. Katzer, N. Nepal, B. P. Downey, D. A. Muller, H. G. Xing, D. J. Meyer, and D. Jena, GaN/NbN epitaxial semiconductor/superconductor heterostructures, Nature **555**, 183 (2018).

[5] E. Müller-Hartmann and J. Zittartz, Kondo Effect in Superconductors, Phys. Rev. Lett. **26**, 428 (1971).

[6] A. Abrikosov and L. Gorkov, Contribution to the theory of superconducting alloys with paramagnetic impurities, Sov. Phys. JEPT **12**, 1243 (1961).

[7] F. Pierre, A. B. Gougam, A. Anthore, H. Pothier, D. Esteve, and Norman O. Birge, Dephasing of electrons in mesoscopic metal wires, Phys. Rev. B **68**, 085413 (2003).

[8] J. Vranken, C. Van Haesendonck, and Y. Bruynseraede, Enhanced magnetic surface scattering of weakly localized electrons, Phys. Rev. B **37**, 8502 (1988).

[9] F. Pierre and N. O. Birge, Dephasing by Extremely Dilute Magnetic Impurities Revealed by Aharonov-Bohm Oscillations, Phys. Rev. Lett. **89**, 206804 (2002).

[10] A. Rogachev, T.-C. Wei, D. Pekker, A. T. Bollinger, P. M. Goldbart, and A. Bezryadin, Magnetic-field Enhancement of Superconductivity in Ultranarrow Wires, Phys. Rev. Lett. **97**, 137001 (2006).

[11] T. Proslier, J. F. Zasadzinski, L. Cooley, C. Antoine, J. Moore, J. Norem, M. Pellin, and K. E. Gray, Tunneling study of cavity grade Nb: Possible magnetic scattering at the surface, Appl. Phys. Lett. **92**, 212505 (2008).

[12] S. M. Anton, J. S. Birenbaum, S. R. O'Kelley, V. Bolkhovsky, D. A. Braje, G. Fitch, M. Neeley, G. C. Hilton, H.-M. Cho, K. D. Irwin, F. C. Wellstood, W. D. Oliver, A. Shnirman, and J. Clarke, Magnetic Flux Noise in DC SQUIDs: Temperature and Geometry Dependence, Phys. Rev. Lett. **110**, 147002 (2013).

[13] P. Kumar, S. Sendelbach, M. A. Beck, J. W. Freeland, Zhe Wang, Hui Wang, Clare C. Yu, R. Q. Wu, D. P. Pappas, and R. McDermott, Origin and Reduction of $1/f$ Magnetic Flux Noise in Superconducting Devices, Phys. Rev. Appl. **6**, 041001 (2016).

[14] J. S. Chawla, X. Y. Zhang, and D. Gall, Effective electron mean free path in TiN(001), J. Appl. Phys. **113**, 063704 (2013).

[15] H. Leduc, B. Bumble, P. Day, B. Eom, J. Gao, S. Golwala, B. Mazin, S. McHugh, A. Merrill, D. Moore, O. Noroozian, A. Turner, and J. Zmuidzinas, Titanium nitride films for ultrasensitive microresonator detectors, Appl. Phys. Lett. **97**, 102509 (2010).

[16] S. Ohya *et al.*, Room temperature deposition of sputtered TiN films for superconducting coplanar waveguide resonators, Supercond. Sci. Technol. **27**, 015009 (2014).

[17] K. Makise, R. Sun, H. Terai, and Z. Wang, Fabrication and characterization of epitaxial TiN-based Josephson junctions for superconducting circuit applications, IEEE Trans. Appl. Supercond. **25**, 1 (2015).

[18] Y.-C. Tang, H. Zhang, S. Kwon, H. Mohebbi, D. Cory, L.-C. Peng, L. Gu, H.-Z. Guo, K.-J. Jin, and G.-X. Miao, Superconducting resonators based on TiN/tapering/NbN/tapering/TiN heterostructures, Adv. Eng. Mater. **18**, 1816 (2016).

[19] B. Foxen *et al.*, Qubit compatible superconducting interconnects, Quantum Sci. Technol. **3**, 014005 (2017).

[20] M. R. Vissers, J. Gao, D. S. Wisbey, D. A. Hite, C. C. Tsuei, A. D. Corcoles, M. Steffen, and D. P. Pappas, Low loss superconducting titanium nitride coplanar waveguide resonators, Appl. Phys. Lett. **97**, 232509 (2010).

[21] M. Sandberg, M. R. Vissers, J. S. Kline, M. Weides, J. Gao, D. S. Wisbey, and D. P. Pappas, Etch induced microwave losses in titanium nitride superconducting resonators, Appl. Phys. Lett. **100**, 262605 (2012).

[22] J. B. Chang, M. R. Vissers, A. D. Corcoles, M. Sandberg, J. Gao, D. W. Abraham, J. M. Chow, Jay M. Gambetta, M. B. Rothwell, G. A. Keefe, M. Steffen, and D. P. Pappas, Improved superconducting qubit coherence using titanium nitride, Appl. Phys. Lett. **103**, 012602 (2013).

[23] G. Calusine, A. Melville, W. Woods, R. Das, C. Stull, V. Bolkhovsky, D. Braje, D. Hover, D. K. Kim, X. Miloshi, D. Rosenberg, A. Sevi, J. L. Yoder, E. Dauler, and W. D. Oliver, Analysis and mitigation of interface losses in trenched superconducting coplanar waveguide resonators, Appl. Phys. Lett. **112**, 062601 (2018).

[24] S. E. de Graaf, L. Faoro, J. Burnett, A. A. Adamyan, A. Ya. Tzalenchuk, S. E. Kubatkin, T. Lindström, and A. V. Danilov, Suppression of low-frequency charge noise in superconducting resonators by surface spin desorption, Nat. Commun. **9**, 1143 (2018).

[25] E. F. C. Driessen, P. C. J. J. Coumou, R. R. Tromp, P. J. de Visser, and T. M. Klapwijk, Strongly Disordered TiN

and NbTiN *s*-wave Superconductors Probed by Microwave Electrodynamics, Phys. Rev. Lett. **109**, 107003 (2012).
[26] A. M. Finkel'stein, Suppression of superconductivity in homogeneously disordered systems, Phys. B: Condens. Matter **197**, 636 (1994).
[27] V. F. Gantmakher and V. T. Dolgopolov, Superconductor–insulator quantum phase transition, Phys. Usp. **53**, 1 (2010).
[28] C. Delacour, L. Ortega, M. Faucher, T. Crozes, T. Fournier, B. Pannetier, and V. Bouchiat, Persistence of superconductivity in niobium ultrathin films grown on R-plane sapphire, Phys. Rev. B **83**, 144504 (2011).
[29] B. Sacépé, T. Dubouchet, C. Chapelier, M. Sanquer, M. Ovadia, D. Shahar, M. Feigel'man, and L. Ioffe, Localization of preformed Cooper pairs in disordered superconductors, Nat. Phys. **7**, 239 (2011).
[30] T. I. Baturina, S. V. Postolova, A. Yu. Mironov, A. Glatz, M. R. Baklanov, and V. M. Vinokur, Superconducting phase transitions in ultrathin TiN films, EPL (Europhys. Lett.) **97**, 17012 (2012).
[31] D. Shah, H. Reddy, V. Shalaev, and A. Boltasseva, Optical properties of plasmonic ultrathin TiN films, Adv. Opt. Mater. **5**, 1700065 (2017).
[32] G. V. Naik, J. L. Schroeder, X. Ni, A. V. Kildishev, T. D. Sands, and A. Boltasseva, Titanium nitride as a plasmonic material for visible and near-infrared wavelengths, Opt. Mater. Express **2**, 478 (2012).
[33] N. Kinsey, M. Ferrera, G. V. Naik, V. E. Babicheva, V. M. Shalaev, and A. Boltasseva, Experimental demonstration of titanium nitride plasmonic interconnects, Opt. Express **22**, 12238 (2014).
[34] See Supplemental Material at http://link.aps.org/supplemental/10.1103/PhysRevApplied.12.054001 for details on the XPS analysis of TiN films, transport data for TiN films from set 2, analysis of the grain effects on residual resistivity, analysis of the temperature dependence on resistivity, and estimation of Fermi velocity.
[35] A. V. Lubenchenko, A. A. Batrakov, A. B. Pavolotsky, O. I. Lubenchenko, and D. A. Ivanov, XPS study of multilayer multicomponent films, Appl. Surf. Sci. **427**, 711 (2018).
[36] J. M. Ziman, *Electrons and Phonons: The Theory of Transport Phenomena in Solids* (Oxford University Press, New York, 2001).
[37] W. Spengler, R. Kaiser, A. N. Christensen, and G. Müller-Vogt, Raman scattering, superconductivity, and phonon density of states of stoichiometric and nonstoichiometric TiN, Phys. Rev. B **17**, 1095 (1978).
[38] A. Torgovkin, S. Chaudhuri, A. Ruhtinas, M. Lahtinen, T. Sajavaara, and I. J. Maasilta, High quality superconducting titanium nitride thin film growth using infrared pulsed laser deposition, Supercond. Sci. Technol. **31**, 055017 (2018).
[39] B. Sacépé, C. Chapelier, T. I. Baturina, V. M. Vinokur, M. R. Baklanov, and M. Sanquer, Disorder-induced Inhomogeneities of the Superconducting State Close to the Superconductor-insulator Transition, Phys. Rev. Lett. **101**, 157006 (2008).
[40] U. Guler, J. C. Ndukaife, G. V. Naik, A. G. A. Nnanna, A. V. Kildishev, V. M. Shalaev, and A. Boltasseva, Local heating with lithographically fabricated plasmonic titanium nitride nanoparticles, Nano Lett. **13**, 6078 (2013).
[41] C. M. Zgrabik and E. L. Hu, Optimization of sputtered titanium nitride as a tunable metal for plasmonic applications, Opt. Mater. Express **5**, 2786 (2015).
[42] M. L. Roukes, M. R. Freeman, R. S. Germain, R. C. Richardson, and M. B. Ketchen, Hot Electrons and Energy Transport in Metals at Millikelvin Temperatures, Phys. Rev. Lett. **55**, 422 (1985).
[43] P. B. Allen, Theory of Thermal Relaxation of Electrons in Metals, Phys. Rev. Lett. **59**, 1460 (1987).
[44] K. Fuchs, The conductivity of thin metallic films according to the electron theory of metals, Math. Proc. Cambridge Philos. Soc. **34**, 100 (1938).
[45] E. H. Sondheimer, The mean free path of electrons in metals, Adv. Phys. **1**, 1 (1952).
[46] L. Vertchenko, L. Leandro, E. Shkondin, O. Takayama, I. Bondarev, N. Akopian, and A. Lavrinenko, Cryogenic characterization of titanium nitride thin films, Opt. Mater. Express **9**, 2117 (2019).
[47] A. F. Mayadas, M. Shatzkes, and J. F. Janak, Electrical resistivity model for polycrystalline films: The case of specular reflection at external surfaces, Appl. Phys. Lett. **14**, 345 (1969).
[48] E. H. Hwang and S. Das Sarma, Linear-in-T resistivity in dilute metals: A Fermi liquid perspective, Phys. Rev. B **99**, 085105 (2019).
[49] A. A. Varlamov, A. Galda, and A. Glatz, Fluctuation spectroscopy: From Rayleigh-Jeans waves to Abrikosov vortex clusters, Rev. Mod. Phys. **90**, 015009 (2018).
[50] A. M. Finkel'shtein, in *30 Years of the Landau Institute – Selected Papers* (World Scientific Pub Co Inc., Singapore, 1996), p. 288.
[51] O. Bourgeois, A. Frydman, and R. C. Dynes, Proximity effect in ultrathin Pb/Ag multilayers within the Cooper limit, Phys. Rev. B **68**, 092509 (2003).
[52] J. W. P. Hsu, S. I. Park, G. Deutscher, and A. Kapitulnik, Superconducting transition temperature in a Nb/Nb_xSi_{1-x} bilayer, Phys. Rev. B **43**, 2648 (1991).
[53] A. Ludwig and M. J. Zuckermann, The dependence of the superconducting critical temperature of dilute magnetic alloys on impurity concentration, J. Phys. F: Metal Phys. **1**, 516 (1971).
[54] H. Allmaier, L. Chioncel, and E. Arrigoni, Titanium nitride: A correlated metal at the threshold of a Mott transition, Phys. Rev. B **79**, 235126 (2009).
[55] R. H. Koch, D. P. DiVincenzo, and J. Clarke, Model for $1/f$ Flux Noise in SQUIDs and Qubits, Phys. Rev. Lett. **98**, 267003 (2007).
[56] S. Sendelbach, D. Hover, M. Mück, and R. McDermott, Complex Inductance, Excess Noise, and Surface Magnetism in dc SQUIDs, Phys. Rev. Lett. **103**, 117001 (2009).
[57] T. Proslier, M. Kharitonov, M. Pellin, J. Zasadzinski, and G. Ciovati, Evidence of surface paramagnetism in niobium and consequences for the superconducting cavity surface impedance, IEEE Trans. Appl. Supercond. **21**, 2619 (2011).
[58] S. Zhou, E. Čižmár, K. Potzger, M. Krause, G. Talut, M. Helm, J. Fassbender, S. A. Zvyagin, J. Wosnitza, and H. Schmidt, Origin of magnetic moments in defective TiO_2 single crystals, Phys. Rev. B **79**, 113201 (2009).

[59] N. H. Hong, J. Sakai, N. Poirot, and V. Brizé, Room-temperature ferromagnetism observed in undoped semiconducting and insulating oxide thin films, Phys. Rev. B **73**, 132404 (2006).

[60] S. D. Yoon, Y. Chen, A. Yang, T. L. Goodrich, Xu Zuo, D. A. Arena, K. Ziemer, C. Vittoria, and V. G. Harris, Oxygen-defect-induced magnetism to 880 K in semiconducting anatase TiO_{2-x} films, J. Phys.: Condens. Matter **18**, L355 (2006).

[61] G. Drera, Electronic structure of TiO_2 thin films and $LaAlO_3$-$SrTiO_3$ heterostructures: The role of titanium 3d1 states in magnetic and transport properties, Ph.D. thesis, Univ. of Milan, Milan (2011).

[62] G. Drera, M. C. Mozzati, P. Galinetto, Y. Diaz-Fernandez, L. Malavasi, F. Bondino, M. Malvestuto, and L. Sangaletti, Enhancement of room temperature ferromagnetism in N-doped TiO_{2-x} rutile: Correlation with the local electronic properties, Appl. Phys. Lett. **97**, 1 (2010).

[63] S. Gupta, A. Moatti, A. Bhaumik, R. Sachan, and J. Narayan, Room-temperature ferromagnetism in epitaxial titanium nitride thin films, Acta Mater. **166**, 221 (2019).